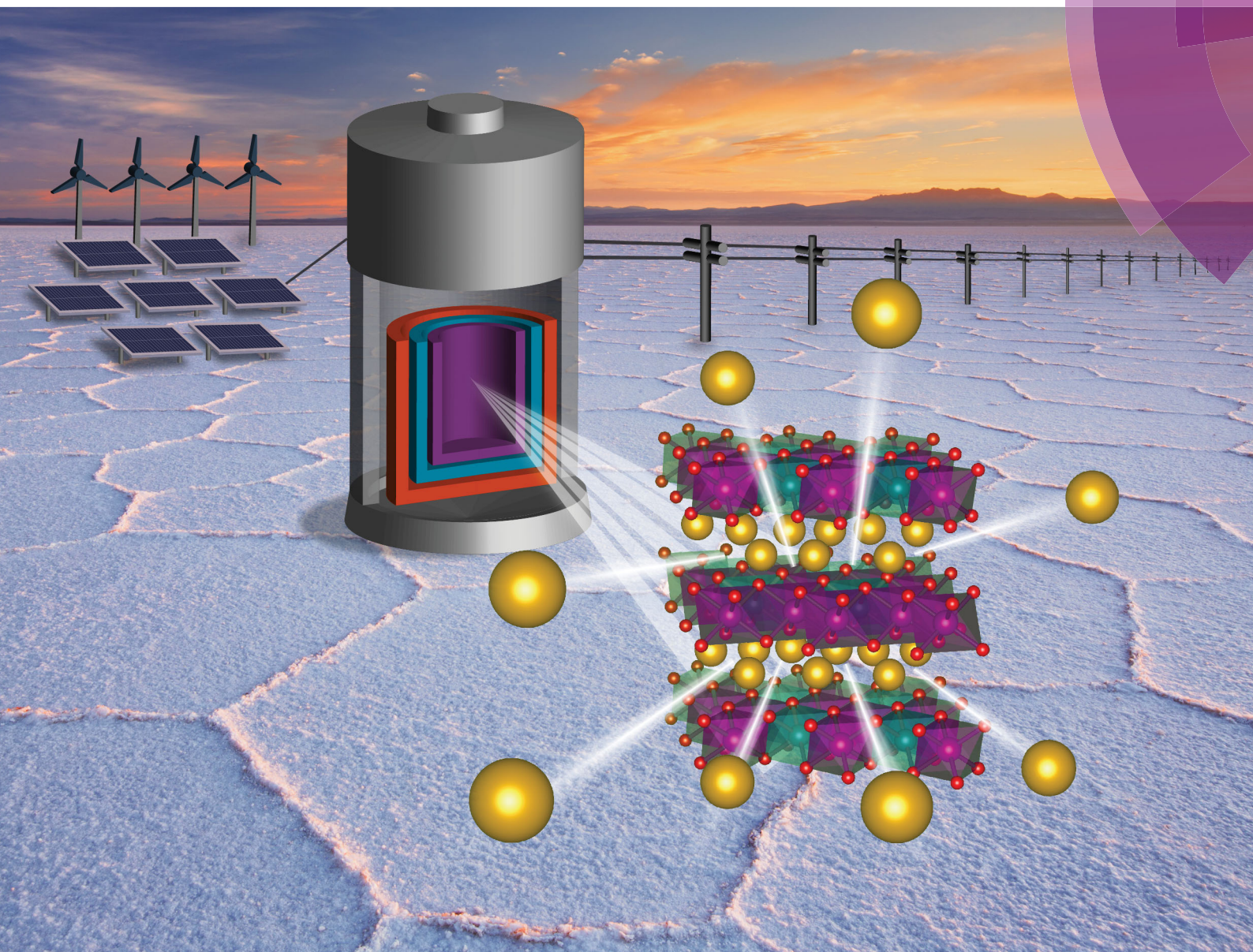


# Energy & Environmental Science

rsc.li/ees



ISSN 1754-5706



**PAPER**

Nuria Tapia-Ruiz, Peter G. Bruce *et al.*  
High voltage structural evolution and enhanced Na-ion diffusion  
in  $\text{P2-Na}_{2/3}\text{Ni}_{1/3-x}\text{Mg}_x\text{Mn}_{2/3}\text{O}_2$  ( $0 \leq x \leq 0.2$ ) cathodes from diffraction,  
electrochemical and *ab initio* studies

Cite this: *Energy Environ. Sci.*,  
2018, 11, 1470

# High voltage structural evolution and enhanced Na-ion diffusion in P2-Na<sub>2/3</sub>Ni<sub>1/3-x</sub>Mg<sub>x</sub>Mn<sub>2/3</sub>O<sub>2</sub> (0 ≤ x ≤ 0.2) cathodes from diffraction, electrochemical and *ab initio* studies†

Nuria Tapia-Ruiz,<sup>a</sup> Wesley M. Dose,<sup>b</sup> Neeraj Sharma,<sup>b</sup> Hungru Chen,<sup>c</sup>  
Jennifer Heath,<sup>c</sup> James W. Somerville,<sup>a</sup> Urmimala Maitra,<sup>a</sup> M. Saiful Islam<sup>c</sup>  
and Peter G. Bruce<sup>a</sup>

We have presented a detailed investigation of the effects of Mg substitution on the structure, electrochemical performance and Na-ion diffusion in high voltage P2-type Na<sub>2/3</sub>Ni<sub>1/3-x</sub>Mg<sub>x</sub>Mn<sub>2/3</sub>O<sub>2</sub> (0 < x < 0.2) cathode materials for Na-ion batteries. Structural analysis using neutron diffraction showed that Mg<sup>2+</sup> substitutes at Ni<sup>2+</sup> sites from ordered [(Ni<sup>2+</sup>/Mn<sup>4+</sup>)O<sub>6</sub>] honeycomb units along the *ab*-plane, leading to an AB-type structure that can be indexed using the P6<sub>3</sub> space group. Within the sodium layers, high Mg-substitution levels (*i.e.* x = 0.2) caused a disruption in the typical Na zig-zag ordering observed in the undoped material, leading to a more disordered Na distribution in the layers. Load curves of the x = 0.1 and 0.2 materials show smooth electrochemistry, indicative of a solid-solution process. Furthermore, DFT calculations showed an increase in Na-ion diffusivity for the Mg-substituted samples. Enhanced cycling stability was also observed in these materials; structural analysis using high-resolution *in operando* synchrotron X-ray diffraction show that such an improved electrochemical performance is caused by the suppression of the O2 phase and switch to the formation of an OP4 phase. *Ab initio* studies support our experimental evidence showing that the OP4 phase (*cf.* O2) is the most thermodynamically stable phase at high voltages for Mg-substituted compounds. Finally, we have provided evidence using diffraction for the x = 1/2 and x = 1/3 intermediate Na<sup>+</sup>-vacancy ordered phases in P2-Na<sub>2/3</sub>Ni<sub>1/3</sub>Mn<sub>2/3</sub>O<sub>2</sub>.

Received 18th October 2017,  
Accepted 12th March 2018

DOI: 10.1039/c7ee02995k

rsc.li/ees

## Broader context

Currently, lithium-ion batteries dominate the world of mobile electronics and the electric vehicle market. However, there are concerns about the future cost of lithium due to its increasing demand. For this reason, researchers are developing battery technologies based on new chemistries, especially for applications where size/cost is pivotal (*e.g.* grid storage). Amongst the potential candidates, sodium-ion batteries are attracting much attention because of their abundance, environmental-friendliness and low price. Whilst these requirements may be easily met when designing cathode materials with careful tailoring of transition metals and dopants, there is still a quest to find suitable cathode materials with high energy densities and high power (*i.e.* comparable to Li-ion cathodes) that may operate during long cycle times.

## Introduction

Lithium-ion batteries have helped in the worldwide revolution in portable electronics due to their high-energy density.

However, there are serious concerns about the cost of lithium due to its scarcity and geographically-concentrated availability. In this context, sodium-ion batteries have emerged as a promising alternative, especially when volumetric and gravimetric energy density requirements are not as stringent, *e.g.* grid storage, thereby addressing the issues related to cost and supply.<sup>1,2</sup>

Sodium-ion batteries based on layered oxide compounds with general formula Na<sub>x</sub>TMO<sub>2</sub> (TM = transition metal) adopting P2-type and O3-type structures<sup>3</sup> have become strong contenders for application. In these structures, P and O refer to the Na coordination, *i.e.* trigonal prismatic or octahedral, respectively,

<sup>a</sup> Department of Materials and Chemistry, University of Oxford, Parks Road, Oxford OX1 3PH, UK. E-mail: n.tapia.ruiz@lancaster.ac.uk, peter.bruce@materials.ox.ac.uk

<sup>b</sup> School of Chemistry, UNSW Australia, Sydney 2052, Australia

<sup>c</sup> Department of Chemistry, University of Bath, Bath BA2 7AY, UK

† Electronic supplementary information (ESI) available. See DOI: 10.1039/c7ee02995k

while the numerals designate the repeated transition metal oxide stacking within the unit cell (ABBA and ABCABC for “2” and “3”, respectively). Layered P2-type compounds have shown enhanced electrochemical performance as they generally undergo fewer structural transitions when (de)intercalating Na-ions compared to O3.<sup>1</sup> In particular, P2-Na<sub>2/3</sub>Ni<sub>1/3</sub>Mn<sub>2/3</sub>O<sub>2</sub> has shown promise due to its high theoretical capacity (*ca.* 170 mA h g<sup>-1</sup>) and high average voltage (*ca.* 3.5 V) because of the presence of the active Ni<sup>2+</sup>/Ni<sup>4+</sup> redox couple. However, the material possesses poor cycle life, which has been attributed to the gliding of the transition metal layers at high voltages and subsequent formation of the O2 phase.<sup>4,5</sup> In addition, the plateaux occurring upon charge/discharge have been attributed to specific sodium ordering patterns in the edge-shared and face-shared sodium sites when the sodium contents are 1/2 and 1/3.<sup>6</sup>

Sodium ordered compounds are thermodynamically more stable than their disordered counterparts, impeding Na<sup>+</sup> mobility, which results in poorer performance at high current rates.<sup>6,7</sup> To date, researchers have made considerable efforts to improve the electrochemical performance of P2-Na<sub>2/3</sub>Ni<sub>1/3</sub>Mn<sub>2/3</sub>O<sub>2</sub> by strategic doping of this material with selected cations, namely Li<sup>+</sup>, Cu<sup>2+</sup>, Al<sup>3+</sup>, Zn<sup>2+</sup> and Ti<sup>4+</sup>.<sup>8–12</sup> Mg<sup>2+</sup> substitution for Ni<sup>2+</sup> has shown great promise and hence is one of the most studied approaches,<sup>12,13</sup> although the non-redox active behaviour of Mg<sup>2+</sup> in principle causes a penalty on the overall charge stored in the material. However, there is still a need for greater fundamental understanding of the important effects: the structural role of Mg in the Ni<sup>2+</sup>/Mn<sup>4+</sup> honeycomb layers (along the *ab* plane) and *c* axis, and how its presence/absence affects the Na<sup>+</sup>-vacancy order/disorder in these materials and the phases obtained at the end of charge. A more complete understanding of this behaviour will allow us to design battery materials with promising electrochemical performance in terms of cyclability and rate capability.

In this study, a series of P2-type Na<sub>2/3</sub>Ni<sub>1/3-x</sub>Mg<sub>x</sub>Mn<sub>2/3</sub>O<sub>2</sub> (0 ≤ *x* ≤ 0.2) materials were prepared by a conventional solid-state method and were structurally characterised using mainly X-ray and neutron diffraction techniques. Cycling data was performed in half-cells *vs.* Na at room temperature. *Ab initio* simulation studies were conducted to examine structural and Na-ion diffusion properties on Mg substitution, complementing the experimental insights.

## Results and discussion

### Crystal structure

P2-Na<sub>2/3</sub>Ni<sub>1/3-x</sub>Mg<sub>x</sub>Mn<sub>2/3</sub>O<sub>2</sub> materials (where 0 ≤ *x* ≤ 0.2) were synthesised from their respective oxides *via* solid-state methods. Elemental analysis from inductively coupled plasma (ICP) spectroscopy confirms the compositions are as targeted (Table S1, ESI<sup>†</sup>). Particles of 1–10 μm of diameter and hundreds of nanometers of thickness and hexagonal morphologies were observed (Fig. S1, ESI<sup>†</sup>). Powder X-ray diffraction (PXRD) was used to confirm the purity of the samples (Fig. S2, ESI<sup>†</sup>). All Bragg reflections from each individual sample could be assigned to a P2-type layered structure with *P*6<sub>3</sub>/*mmc* (no. 194) space group.

The lattice parameters for the P2-Na<sub>2/3</sub>Ni<sub>1/3</sub>Mn<sub>2/3</sub>O<sub>2</sub> sample are comparable to those reported in the literature.<sup>5</sup> A broad reflection at *d* = 4.2 Å (1/3 1/3 0) (not shown here) was observed in the Mg-containing samples, corresponding to long-range in-plane ordering represented by [(Mg<sup>2+</sup>/Mn<sup>4+</sup>)O<sub>6</sub>] honeycomb units (in a √3a × √3a type supercell).<sup>14</sup> As expected, this Bragg reflection becomes more significant at high levels of Mg. The Mg<sup>2+</sup>/Mn<sup>4+</sup> honeycomb-type ordering occurs due to the large differences in radii and charge (*ca.* Mg<sup>2+</sup>/Mn<sup>4+</sup> = 1.38). By contrast, elucidation of Ni<sup>2+</sup>/Mn<sup>4+</sup> ordering, which is analogous to the Mg<sup>2+</sup>/Mn<sup>4+</sup> ordering, was easily evidenced using neutron diffraction (ND) due to their different neutron scattering lengths (see Experimental section). A comparison between X-ray and neutron diffraction data for the P2-Na<sub>2/3</sub>Ni<sub>1/3</sub>Mn<sub>2/3</sub>O<sub>2</sub> sample is shown in Fig. 1a.

ND data at room temperature for the P2-Na<sub>2/3</sub>Ni<sub>1/3-x</sub>Mg<sub>x</sub>Mn<sub>2/3</sub>O<sub>2</sub> (0 ≤ *x* ≤ 0.2) series are shown in Fig. 1b and c. Selected Rietveld refined crystallographic parameters from ND data are presented in the ESI.<sup>†</sup> An increase in the lattice parameters was observed upon Mg-replacement due to the slightly larger size of Mg<sup>2+</sup> (0.72 Å) when compared to Ni<sup>2+</sup> (0.69 Å) in octahedral coordination. The cell parameters of Na<sub>2/3</sub>Ni<sub>1/3</sub>Mn<sub>2/3</sub>O<sub>2</sub> are in good agreement with those from X-ray data and the literature.<sup>5</sup> Data were refined using the Rietveld method using an AB-type crystallographic model (*P*6<sub>3</sub> space group).<sup>15,16</sup> This structural model considers a larger hexagonal unit cell than that described by the *P*6<sub>3</sub>/*mmc* space group, with in-plane [(Ni<sup>2+</sup>/Mg<sup>2+</sup>)/Mn<sup>4+</sup>]O<sub>6</sub> honeycomb stacking layers which are not superimposed along the *c*-axis, hence the A–B nomenclature. This superstructure differs from the AA-type, reported in the Na<sub>2/3</sub>Mg<sub>1/3</sub>Mn<sub>2/3</sub>O<sub>2</sub> material by Paulsen *et al.*,<sup>16</sup> where honeycomb ordered layers overlay along the *c* axis.<sup>16</sup> In our model, we have considered that Ni<sup>2+</sup> and Mg<sup>2+</sup> ions are located at the same octahedral 2b sites due to their identical pristine charge and relatively similar sizes, whereas Mn<sup>4+</sup> atoms are located in both 2a and 2b sites in the MO<sub>2</sub> layers; larger Na ions are located in between MO<sub>2</sub> layers in trigonal prismatic sites (*i.e.* 6c sites predominantly (*ca.* 75% Na available) as these correspond to the more stable edge sites and in a lower amount in the face-shared 2a and 2b sites). In-plane and inter-plane ordering patterns are characterised by the reflections observed in the 3.4 < *d* < 4.5 Å range (Fig. 1c).<sup>15</sup> In-plane Ni(Mg)/Mn long-range ordering is characterised by the 010 and 012 reflections at 4.35 and 3.45 Å respectively, whereas intraplane Ni(Mg)/Mn long-range ordering is characterised by the 011 reflection at 4.1 Å. These peaks have been indicated in Fig. 1c with a (\*) sign and are still present in the ND data, even at the largest magnesium content. The AA-type structure differs from the AB-type structure on the absence of the reflection at 4.1 Å.<sup>15</sup>

The reflections at *d* = 3.15 and 3.25 Å are coincident to those observed by Meng *et al.*<sup>6</sup> when describing the large zig-zag (LZZ)-sodium ordering in prismatic sites on [P2-Na<sub>2/3</sub>Ni<sub>1/3</sub>Mn<sub>2/3</sub>O<sub>2</sub>] (Fig. 1c). However, it was not possible to observe in these data the Bragg reflection at *ca.* 3.04 Å reported by Meng *et al.*<sup>6</sup> These reflections broaden at the highest Mg content studied here, *i.e.* *x* = 0.2 (data shown in pink in Fig. 1c). Two extra peaks (marked with a (+) sign) were observed in this sample in the *d* spacing range studied. These peaks were matched to a second

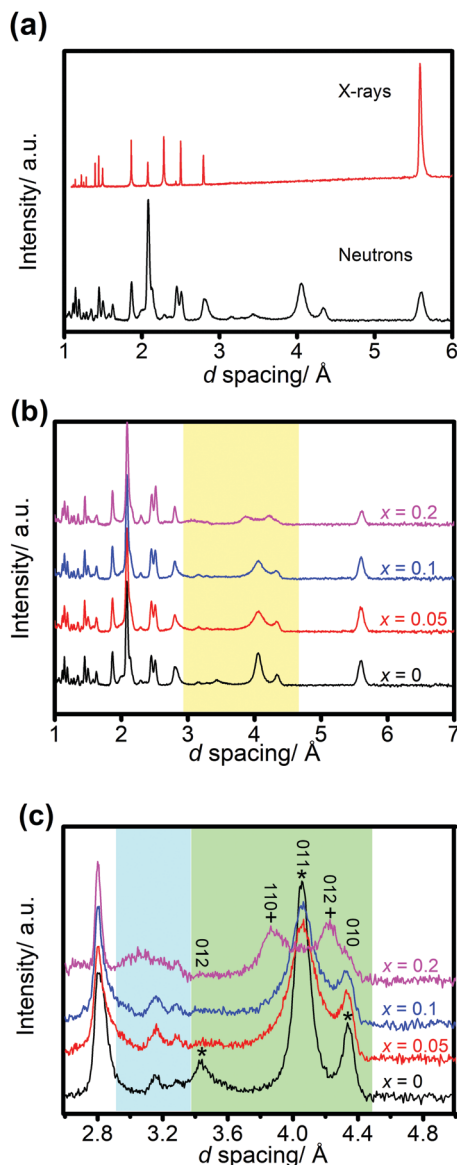


**Fig. 1** (a) X-ray and neutron diffraction data comparison for  $\text{Na}_{2/3}\text{Ni}_{1/3-x}\text{Mg}_x\text{Mn}_{2/3}\text{O}_2$ , where  $x = 0$ ; (b) stacked plots showing neutron diffraction data for  $\text{Na}_{2/3}\text{Ni}_{1/3-x}\text{Mg}_x\text{Mn}_{2/3}\text{O}_2$ , where  $0 \leq x \leq 0.2$ . Yellow-highlighted region represents the  $d$  spacing range where ordering features related to sodium and magnesium/transition metal atoms have been observed; and (c) zoom of the yellow-highlighted region in Fig. 1b. Blue-highlighted area shows evolution of peaks related to the zig-zag Na ordered distribution upon Mg concentration. Green-highlighted area shows peaks attributed to inter-plane and intra-plane magnesium/transition metal ordering in the main phase. (\*) indicates  $hkl$  reflections indexed using  $P6_3$  the space group (no. 173); and (+) indicates  $hkl$  reflections indexed using the  $P6_3/m$  space group (no. 176).

phase (ca. 20 wt%) that could be refined as a  $\sqrt{7}a \times \sqrt{7}a$ -type ordered superstructure with hexagonal space group  $P6_3/m$  (no. 176), isostructural to  $\text{K}_4\text{Co}_7\text{O}_{14}$ , and with lattice parameters  $a = 7.706(3)$  Å and  $c = 11.051(6)$  Å. This structural model was previously used by Imanishi *et al.* to describe a unique Na ordering in the  $\text{Na}_{0.58}\text{CoO}_2$  structure, with Na atoms in two inequivalent Na sites (2b and 6h) which induce a shift of the Co-atom trimers parallel to the  $c$ -axis.<sup>18</sup>

### Electrochemical performance in Na-half cells

Charge/discharge galvanostatic curves of the  $\text{P2-Na}_{2/3}\text{Ni}_{1/3-x}\text{Mg}_x\text{Mn}_{2/3}\text{O}_2$  ( $0 \leq x \leq 0.2$ ) samples in the voltage range 2–4.5 V are shown in Fig. 2a. The experimental capacities obtained in  $\text{P2-Na}_{2/3}\text{Ni}_{1/3}\text{Mn}_{2/3}\text{O}_2$  are comparable to those reported in the literature.<sup>5,6</sup> Contrary to our calculations where we consider exclusively the electrochemical oxidation of  $\text{Ni}^{2+}$  (found in the pristine materials using XANES (Fig. S7, ESI†)) to  $\text{Ni}^{4+}$ , we have observed experimental capacities larger than expected in the magnesium substituted samples. Here, we have assumed that the  $\text{Mn}^{4+}$  observed by XANES in the pristine materials does not have any electrochemical activity, *i.e.* does not oxidise to  $\text{Mn}^{5+}$  as described in other reports from Mn-containing compounds.<sup>17</sup> This behaviour is notably more significant when  $x = 0.2$ , where an extra 38 mA h  $\text{g}^{-1}$  was achieved on the first charge.

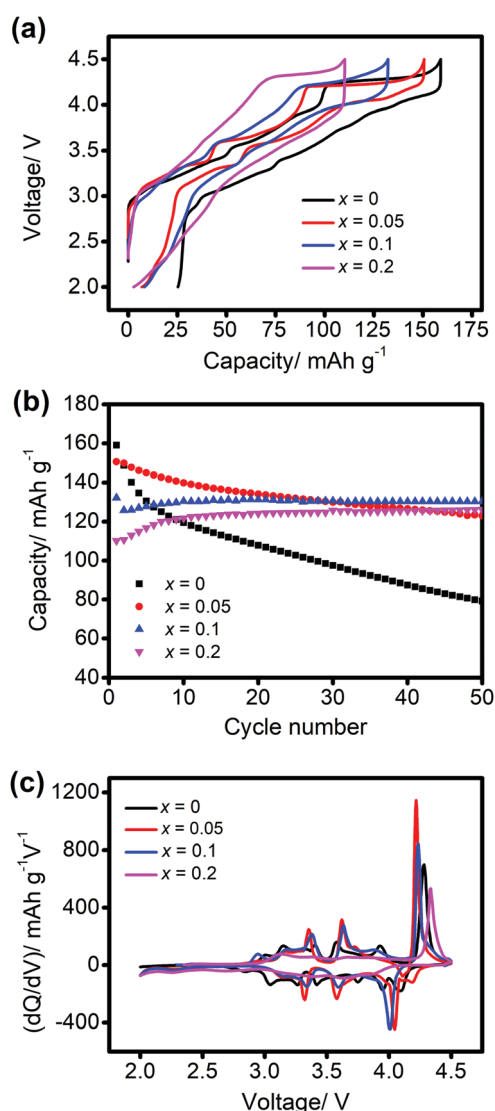


**Fig. 2** First charge and discharge curves for  $\text{Na}_{2/3}\text{Ni}_{1/3-x}\text{Mg}_x\text{Mn}_{2/3}\text{O}_2$ , where  $0 \leq x \leq 0.2$ , in the voltage range 2–4.5 V at  $10 \text{ mA g}^{-1}$ ; (b) discharge cycling data (up to 50 cycles) for samples shown in Fig. 1; and (c) differential capacity curves for data shown in (a).

Similar electrochemical behaviour was reported by Yabuuchi *et al.* in  $\text{P2-Na}_{0.67}\text{Mg}_{0.28}\text{Mn}_{0.72}\text{O}_2$  and their explanation for the abnormally high capacity (about 100 extra  $\text{mA h g}^{-1}$ ) was attributed to oxygen participation.<sup>14</sup>

The replacement of  $\text{Ni}^{2+}$  by  $\text{Mg}^{2+}$  ions favours the initial capacity retention on cycling,<sup>12,13</sup> with a higher cycling efficiency when  $x \geq 0.1$  (Fig. 2b). A slight increase in discharged specific capacities was observed in the first 20 cycles for the  $x \geq 0.1$  samples, although this effect is more pronounced in the  $x = 0.2$  sample. In this cycle range, the specific capacities increased by 4.5% and 12.6% for  $x = 0.1$  and  $x = 0.2$  samples, respectively.  $dQ/dV$  plots were used to further study the increase in capacity in these samples, which revealed an irreversible high voltage feature occurring at *ca.* 3.9 V upon increased cycling (Fig. S8, ESI†). The enhanced capacity retention in magnesium-substituted samples compared to the  $\text{P2-Na}_{2/3}\text{Ni}_{1/3}\text{Mn}_{2/3}\text{O}_2$  material has been explained by the switch from the detrimental O2 phase, observed in this material at high voltages, to the intergrowth OP4 phase.<sup>13</sup>

Furthermore, smoother charge and discharge curves were observed upon  $\text{Mg}^{2+}$  substitution (these being optimal when  $x = 0.2$ ), indicating a predominant solid-solution reaction mechanism. This is clearly indicated in the  $dQ/dV$  plots shown in Fig. 2c. Single phase reactions on cycling caused by  $\text{Na}^+$  vacancy disorder have been related to high  $\text{Na}^+$  conductivity and excellent high-rate electrochemical performance.<sup>7</sup> Structural changes upon cycling of these samples were then analysed by *in operando* diffraction methods described in the next section.

### Structural evolution from *in operando* X-ray diffraction

The structural evolution determined from the *in operando* synchrotron XRD experiments during sodium (de)intercalation in the  $\text{P2-Na}_{2/3}\text{Ni}_{1/3-x}\text{Mg}_x\text{Mn}_{2/3}\text{O}_2$  ( $0 \leq x \leq 0.2$ ) series is shown in Fig. 3 for the (002) and (100) reflections (space group  $P6_3/mmc$ ). Rietveld analysis of the patterns collected before cycling (Tables S7–S9, ESI†) was in good agreement with the powder-only structural models. In general, during charge (sodium removal) the  $00l$  reflections shift to lower angles, an expansion of the  $c$  axis; while the  $h00$  and  $h0l$  reflections shift to higher angles, a contraction in the  $a$  axis. The reverse trends were observed during discharge (sodium insertion), in agreement with those reported previously for  $x = 0$ .<sup>5,6</sup>

**P2- $\text{Na}_{2/3}\text{Ni}_{1/3}\text{Mn}_{2/3}\text{O}_2$  evolution.** Without Mg substitution ( $x = 0$ ) the structure undergoes a series of two-phase reactions during overall expansion and contraction below 4.0 V, and above 4.2 V. As reported in earlier work, the phase transformation from P2 to O2 occurs above 4.2 V on charge and is associated with the 4.28 V plateau.<sup>5,7</sup> Increased repulsion between successive O layers (directly facing each other in the P2 structure (ABBA)) at low sodium content prompts the  $\text{MO}_2$  sheets to glide in the  $a$ - $b$  plane to transform into the O2 structure (ABCB). Total energy calculations have shown this to be the more stable phase after removing all Na ions.<sup>6</sup> Lu and Dahn first proposed that the voltage plateaux at 3.0 and 3.6 V correspond to specific Na ion ordering at  $x = 1/2$  and  $1/3$  respectively.<sup>5</sup> Meng and co-workers<sup>6</sup> used first principles

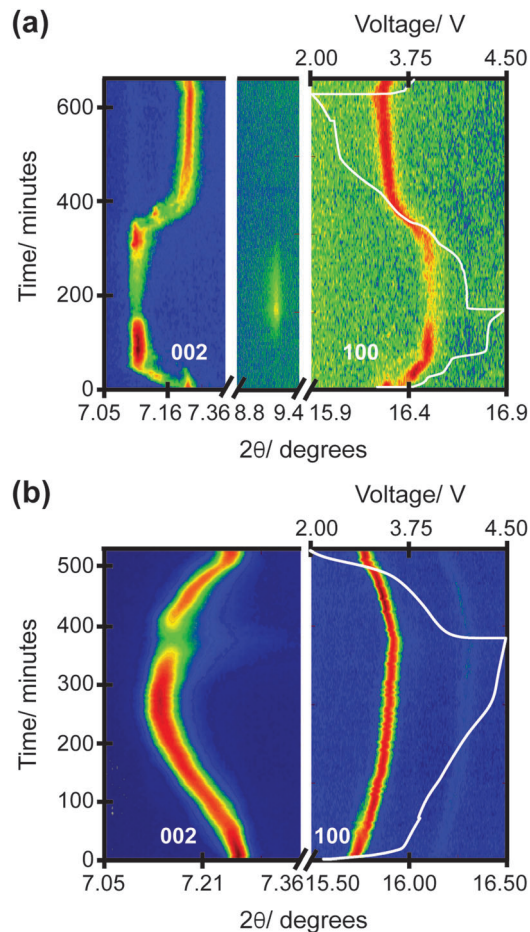


Fig. 3 Selected  $2\theta$  regions of *in operando* synchrotron XRD data highlighting the evolution of the (002) and (100) reflections for  $\text{Na}_{2/3}\text{Ni}_{1/3-x}\text{Mg}_x\text{Mn}_{2/3}\text{O}_2$  where (a)  $x = 0$ ; and (b)  $x = 0.2$ . The colour scale represents reflection intensity and the potential profiles are included.

calculations to model the nature of the ordering and the structure of these intermediate phases.

The high resolution *in operando* synchrotron XRD experiments described in our work provide experimental evidence for the intermediate phases, and demonstrate how these phases evolve with respect to time and voltage. Sequential Rietveld refinements were carried out to determine the lattice parameters and weight fraction of the respective phases (Fig. 4, and details of the fits are given in the ESI†). On charge at  $50 \text{ mA g}^{-1}$  two phases were clearly resolved prior to the P2–O2 phase transition. The new phase appears at 3.5 V, coinciding with the first voltage step, and the lattice parameters of this new phase evolve rapidly ( $a$  decreased while  $c$  increased) through to 3.8 V and the second voltage step, after which they stabilised at their minimum and maximum values, respectively. Discharge (sodium insertion) was performed specifically at a slower rate ( $10 \text{ mA g}^{-1}$ ) to give better resolution of the phase changes, and thus these are discussed in more detail.

Upon sodium insertion, the P2 and O2 phases coexist from the charged state to the end of the 4.0 V plateau. Three P2 phases were observed thereafter, corresponding to the 3.6, 3.0

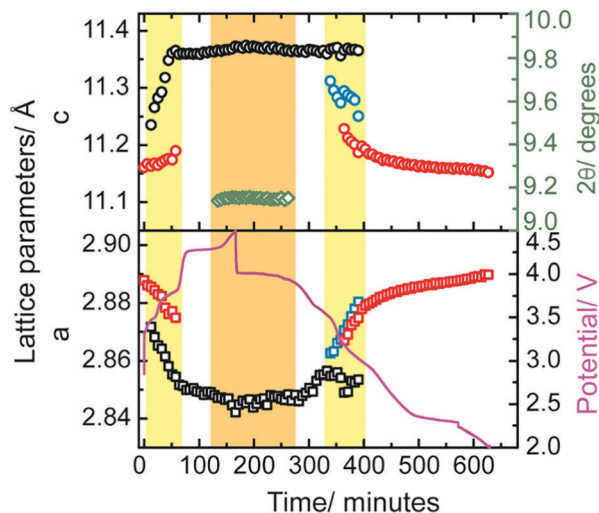


Fig. 4 Changes in *a* and *c* lattice parameters of the  $\text{Na}_{2/3}\text{Ni}_{1/3}\text{Mn}_{2/3}\text{O}_2$  electrode ( $x = 0$ ) during charge–discharge, together with the electrochemical profile. The lattice parameters of the P2 ordered phases are shown in black (1/3 Na), blue (1/2 Na) and red (2/3 Na), and the  $2\theta$  position of the 002 reflection from the O2 phase is shown in green. Error bars are within the symbols. The two yellow shaded regions indicate the phase transitions between P2 sodium ordered structures and the orange shaded region indicates the P2 to O2 phase transition.

and 2.3 V plateaux. The lattice parameters of the three P2 phases (at the maximum phase weight fraction) are compared to the  $x = 1/3$ ,  $1/2$  and  $2/3$  sodium ordered structures reported by Meng and co-workers (*ex situ* data)<sup>6</sup> in Fig. 5. Although Fig. 5 compares the dynamic/metastable structure (this work) with the relaxed/equilibrium structure,<sup>6</sup> there is a good agreement between these data. Therefore, based on the comparisons of the structures and the approximate composition (derived from the electrochemistry), it can be concluded that the intermediate phases observed in our *in operando* work agree with the proposed compositions in the literature. This is the first time that experimental evidence for the Na ion ordered structures are reported and discussed in  $\text{Na}_{2/3}\text{Ni}_{1/3}\text{Mn}_{2/3}\text{O}_2$ , confirming the calculated structures reported previously.<sup>6</sup>

**Effect of Mg substitution above 4 V.** From a visual inspection of the *in operando* synchrotron XRD pattern evolution (Fig. 3) and the electrochemical profiles (Fig. 2a), it is clear that Mg-substitution has had a significant effect on the phase evolution. Adding 10% Mg ( $x = 0.1$ ) was sufficient to suppress the P2 to O2 phase transition, in agreement with Wang *et al.*<sup>19</sup> However, upon sodium removal above 4.3 V we observed a loss of reflection intensity and a broad reflection at  $2\theta = 7.35^\circ$  (Fig. 6), which is not discussed in ref. 19. We identify this phase transition as the P2 to OP4 transition, where the OP4 phase shows alternate stacking of octahedral and trigonal prismatic sodium layers along the *c* axis, as has been previously identified in  $\text{Na}_{2/3}\text{Fe}_{1-y}\text{Mn}_y\text{O}_2$  materials.<sup>20</sup> While substitution of 20% Mg ( $x = 0.2$ ) did not prevent the P2 reflections losing intensity in the charged state, the OP4 reflection was no longer observed in the first charged state (Fig. 6). However, asymmetric broadening of the (002) reflection indicated the presence of stacking faults.

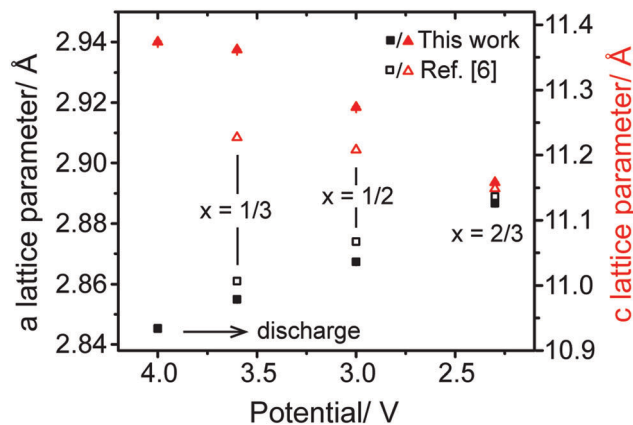


Fig. 5 Comparison of the lattice parameters at the 4.0 V, 3.6 V, 3.0 V and 2.3 V plateaux on discharge collected *in operando* in this work (filled data) with the lattice parameters of the  $x = 1/3$ ,  $1/2$  and  $2/3$  ordered structures (4.0 V, 3.5 V and before charging respectively) collected *ex situ* during charge by Meng and co-workers (open data).<sup>6</sup> Error bars are included within the symbols.

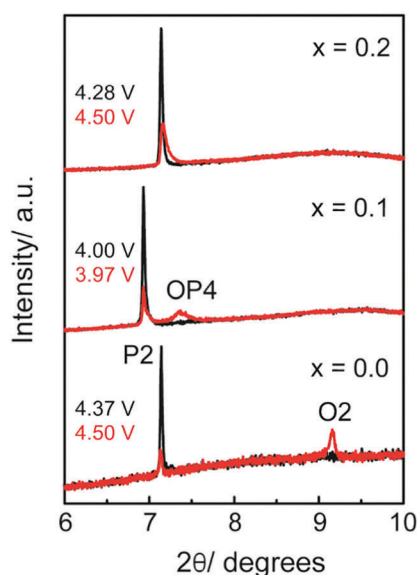


Fig. 6 *In operando* XRD patterns for  $\text{Na}_{2/3}\text{Ni}_{1/3-x}\text{Mg}_x\text{Mn}_{2/3}\text{O}_2$ , where  $0 \leq x \leq 0.2$ , prior to the charged state (black) and in the charged state (red) between  $6^\circ$  and  $10^\circ$   $2\theta$ . The red XRD pattern shown for  $x = 0.1$  is 10 minutes after the charged state (3.97 V) where the OP4 reflection is most intense.

DFT calculations have also shown the inhibition of P2 to O2 phase transformation. Without Mg, all  $\text{Na}^+$  ions can theoretically be extracted from the structure of  $\text{Na}_{2/3}\text{Ni}_{1/3}\text{Mn}_{2/3}\text{O}_2$  at the end of the charge, accompanied by the oxidation of  $\text{Ni}^{2+}$  to  $\text{Ni}^{4+}$ . Empty Na layers then enable the gliding of  $\text{MO}_2$  sheets and results in the transformation from P2 to O2 structures.<sup>5,6,21</sup> In the Mg substituted  $\text{Na}_{2/3}\text{Ni}_{1/3-x}\text{Mg}_x\text{Mn}_{2/3}\text{O}_2$  samples, two  $\text{Na}^+$  ions must stay in the vicinity of a  $\text{Mg}^{2+}$  ion at high voltages (*ca.* 4.2 V), in order to keep the local charge neutrality. This prevents the formation of consecutive empty Na layers and hence the transformation to the O2 structure is inhibited.

Fig. 7 shows two possible local structures around the  $\text{Mg}^{2+}$  ion during the P2–OP4 phase transformation. The first situation,

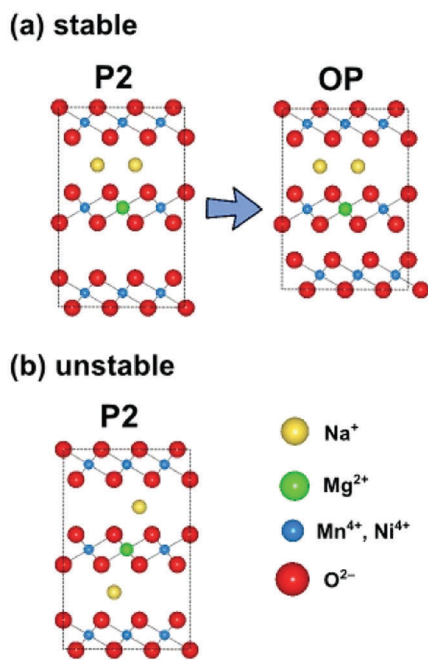


Fig. 7 Two possible local structures around the  $\text{Mg}^{2+}$  ion at 4.2 V. (a) The low energy configuration, where two Na ions are located at the same side of the  $\text{MO}_2$  sheet and the empty Na layer allows the transformation from P stacking to O stacking. (b) The high energy configuration, where two Na ions are located on each side of the  $\text{MO}_2$  sheet.

(a), is where both  $\text{Na}^+$  ions are located on the same side of the  $\text{MO}_2$  sheet and therefore one Na layer is completely empty. The empty layer then enables gliding of  $\text{MO}_2$  sheets resulting in O type stacking. The second situation, (b), is where the two  $\text{Na}^+$  ions are located on each side of the  $\text{MO}_2$  sheet. Our DFT calculations have examined these structures and indicate that the first configuration is more energetically stable, which is consistent with the experimentally observed P2 to OP4 transition in the Mg substituted samples, especially for  $x = 0.1$ .

**Effect of Mg substitution below 4 V.** Mg doping smoothed the charge/discharge profile below 4 V.<sup>19</sup> Comparison of the *in operando* XRD patterns for  $x = 0$  and  $x = 0.1$  revealed that at  $x = 0.1$  subtler P2 to  $\text{P2}_{\text{new}}$  phase changes occur (both showing similar lattice parameters) (Fig. S9, ESI†). These are more distinct at faster cycling rates, with clearer two-phase behaviour observed during charge at  $100 \text{ mA g}^{-1}$  than discharge at  $8.5 \text{ mA g}^{-1}$ . By increasing the Mg fraction to  $x = 0.2$ , however, the two-phase behaviour is replaced by continuous reflection evolution characteristic of a solid solution reaction (Fig. 3b). This correlates with the electrochemical observations of smoother charge/discharge curves and illustrates the “removal” of the ordered structures during charge/discharge. These more gradual structural changes upon Na (de)intercalation have also been observed in  $\text{P2 Na}_{2/3}\text{Mn}_{1-y}\text{Mg}_y\text{O}_2$ ,<sup>22</sup> where *ex situ* <sup>23</sup>Na solid state MAS NMR was used to demonstrate that Mg doping leads to more continuous changes in the Na resonances and to fewer, sharper peaks during the first cycle. The absence of ordered structures or the insertion/extraction reactions *via* disordered states, especially in terms of  $\text{Na}^+$ -vacancy disorder, have been related to high  $\text{Na}^+$  conductivity

and excellent high-rate performance.<sup>7</sup> Our work provides direct evidence for the variation in structural order as a function of Mg concentration with respect to electrochemical processes.

**Effect of Mg substitution on volume change.** As discussed above, Mg substitution gave rise to an overall increase in the unit cell volume. In turn, this results in reduced volume contraction/expansion on sodium extraction/insertion. At  $x = 0.1$  and  $0.2$ , the unit cell contraction of the P2 phase on first charge is over half that of the  $x = 0$  material (vol% contraction of 0.56% and 0.52%, respectively, compared to 1.30% for  $x = 0$ ). The subsequent vol% expansion of the  $x = 0.2$  material (0.11%) is also considerably less than either the  $x = 0$  (0.93%) or  $x = 0.1$  (0.58%) samples. The trend in the volume change with Mg content agrees well with the electrochemical behaviour, where increased Mg levels improve performance.

*In operando* synchrotron XRD data have conclusively revealed that during charge–discharge below 4 V the Na ion ordered intermediates are removed as the Mg concentration increases, which in turn leads to smoother charge/discharge profiles and better electrochemical performance. Additionally, the  $x = 0.1$  sample suppresses the formation of the O2 phase, transitioning instead to the intermediate OP4 structure, while higher Mg concentrations of  $x = 0.2$  appear to minimise the transition to the OP4. This correlates with the dramatic reduction in the volume change during charge/discharge as the Mg concentration is increased. All these structural factors point towards superior electrochemical performance of the Mg-substituted samples.

**Effect of Mg substitution on  $\text{Na}^+$  diffusion.** Na-ion diffusion in P-type layered oxide compounds has been shown to be faster than in O-type compounds.<sup>23,24</sup> Strong in-plane Na–Na interactions makes Na-ion diffusion highly correlated.<sup>23</sup> It is therefore necessary to perform molecular dynamics simulations to probe such diffusion mechanisms and to complement the experimental measurements. The simulated Na diffusion results in  $\text{Na}_{0.56}\text{Ni}_{0.33}\text{Mn}_{0.67}\text{O}_2$  and  $\text{Na}_{0.56}\text{Mg}_{0.11}\text{Ni}_{0.22}\text{Mn}_{0.67}\text{O}_2$  from *ab initio* molecular dynamics (AIMD) simulations are shown as mean square displacements in Fig. 8. In agreement with the galvanostatic intermittent titration technique (GITT) and nuclear magnetic resonance (NMR) measurements on this family of compounds,<sup>13</sup> our simulations suggest that Mg substitution leads to an increase in Na-ion diffusivity. Na diffusion coefficients ( $D_{\text{Na}}$ ) derived from classical MD also predict this increase of Na diffusion with Mg replacement; values of  $2.5 \times 10^{-9} \text{ cm}^2 \text{ s}^{-1}$  and  $1.2 \times 10^{-8} \text{ cm}^2 \text{ s}^{-1}$  (at 300 K) are obtained for  $\text{Na}_{0.56}\text{Ni}_{0.33}\text{Mn}_{0.67}\text{O}_2$  and  $\text{Na}_{0.56}\text{Mg}_{0.11}\text{Ni}_{0.22}\text{Mn}_{0.67}\text{O}_2$  respectively. The enhancement in Na diffusion has been attributed to the enlargement of interlayer spacing upon Mg doping.<sup>25</sup> However, the estimated change in interlayer separation is very small (less than 0.05 Å).

Electrochemical data of  $\text{Na}_{2/3}\text{Ni}_{1/3}\text{Mn}_{2/3}\text{O}_2$  have shown sodium ordering and phase separation (Fig. 2a), which results in rich structural and electronic phase diagrams.<sup>26–29</sup> The electrochemically inactive  $\text{Mg}^{2+}$  (with fixed 2+ charge) and its random distribution over Ni sites can effectively suppress the development of long-range charge ordering within the  $\text{MO}_2$  sheet and hence inhibit long-range sodium ordering (see  $x = 0.2$  experimental case detailed above). As a result, charge and

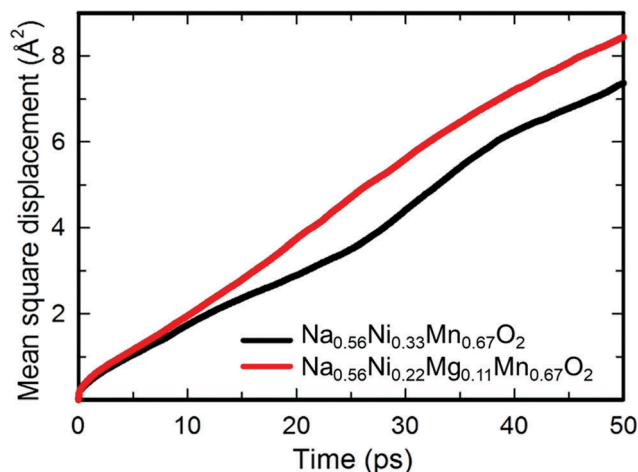


Fig. 8 Mean square displacements of Na ions in  $\text{Na}_{0.56}\text{Ni}_{0.33}\text{Mn}_{0.67}\text{O}_2$  and  $\text{Na}_{0.56}\text{Ni}_{0.22}\text{Mg}_{0.11}\text{Mn}_{0.67}\text{O}_2$  from *ab initio* molecular dynamics (AIMD) simulations at 500 K, indicating faster Na-ion diffusion in the Mg-containing compound.

discharge would proceed through a more solid-solution like reaction with a higher Na-ion diffusivity, as reflected in a more sloping charge–discharge profile (Fig. 2a and 3c). Furthermore, our AIMD simulations on  $\text{Na}_{0.56}\text{Mg}_{0.11}\text{Ni}_{0.22}\text{Mn}_{0.67}\text{O}_2$ , show that the Mg ion displaces in the *z* direction with a larger amplitude than both Ni and Mn, as shown in Fig. 9. This can be attributed to the ionic nature of the Mg–O bond and hence less rigid  $\text{MgO}_6$  octahedra. In contrast, the relatively higher degree of covalency in Ni–O and Mn–O bonds, owing to strong 3d–2p hybridization,<sup>30,31</sup> makes the  $\text{NiO}_6$  and  $\text{MnO}_6$  octahedra more rigid. The large displacement of  $\text{Mg}^{2+}$  in the *z* direction consequently alters the electrostatic potential felt by  $\text{Na}^+$  ions and has a beneficial effect on Na diffusion. An interesting comparison includes a previous NMR study indicating that  $\text{Li}^+$  ions (which have a very similar ionic radius to  $\text{Mg}^{2+}$ ) were

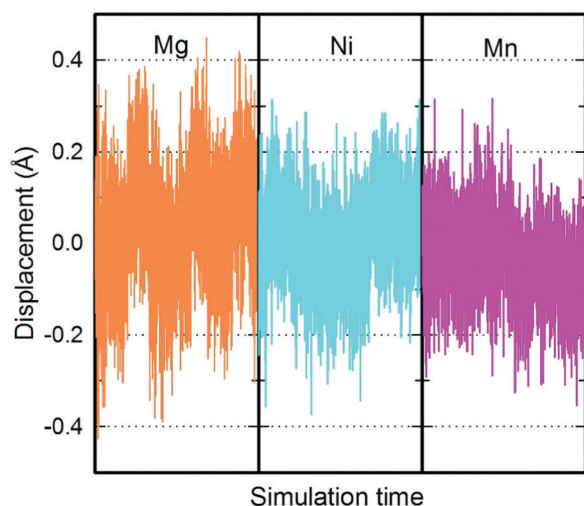


Fig. 9 Displacement of Mg, Ni and Mn ions in the *z*-direction in  $\text{Na}_{0.56}\text{Mg}_{0.11}\text{Ni}_{0.22}\text{Mn}_{0.67}\text{O}_2$  during the 50 ps AIMD simulation at 500 K, indicating larger amplitudes for Mg.

displaced from transition metal layers to the Na layers in the  $\text{P2-Na}_x[\text{Li}_y\text{Ni}_z\text{Mn}_{1-y-z}]\text{O}_2$  material.<sup>21</sup>

## Conclusions

In this work we have demonstrated the effects of Mg substitution on the structure of a series of  $\text{P2-Na}_{2/3}\text{Ni}_{1/3-x}\text{Mg}_x\text{Mn}_{2/3}\text{O}_2$  compounds. Combined XRD and neutron diffraction analysis show that magnesium substitutes nickel in the Ni–Mn honeycomb layers, forming an AB-type structure as in the parent material. Hence there is no structural re-arrangement in the *c*-axis upon Mg substitution. We have also shown that high levels of Mg in the structure (*i.e.*  $x = 0.2$ ) lead to a more disordered distribution of sodium in the pristine material. Electrochemical results corroborate our structural data by showing a solid-solution profile. Importantly, this is the highest level of Mg substitution in the  $\text{P2-Na}_{2/3}\text{Ni}_{1/3-x}\text{Mn}_{2/3}\text{O}_2$  compound reported to date. The high resolution *in operando* synchrotron XRD experiments provide evidence for the  $x = 1/2$  and  $x = 1/3$  intermediate  $\text{Na}^+$ -vacancy ordered phases in  $\text{P2-Na}_{2/3}\text{Ni}_{1/3}\text{Mn}_{2/3}\text{O}_2$ . Furthermore, we have shown that Mg substitution effectively disrupts the  $\text{Na}^+$ -vacancy ordering leading to more gradual structural changes, and suppresses the P2–O2 transition at high voltages, switching it to an OP4 phase. *Ab initio* molecular dynamics studies have indicated that Na-ion diffusivity increases and that the OP4 phase is the most thermodynamically stable phase at high voltages in the Mg-substituted compounds.

The results of this work have shed new light on the role of magnesium in the high-voltage  $\text{P2-Na}_{2/3}\text{Ni}_{1/3}\text{Mn}_{2/3}\text{O}_2$  cathode. Understanding the structural and electrochemical changes occurring in cathode materials when a dopant is added to the system is of paramount importance in the design of novel materials with enhanced electrochemical performance.

## Methods

### Synthesis

Samples were synthesised by ball milling a stoichiometric mixture of  $\text{Na}_2\text{CO}_3$  anhydrous (Fisher Chemicals), NiO (Sigma Aldrich, nanopowder, <50 nm particle size),  $\text{MnO}_2$  (Sigma Aldrich, –325 mesh, 99%) and MgO (Sigma Aldrich, –325 mesh, ≥99% trace metal basis) in acetone in a Planetary Ball Mill PM 100 (Retsch) for 1 h at 450 rpm using a 2 : 1 ball-to-powder-ratio. The mixture was left to dry in air and the powders were pressed as pellets under a load of 4 tons  $\text{cm}^{-2}$  before calcining at 800–850 °C for 12 h in air followed by slow cooling in the furnace. Samples were kept in an argon-filled glovebox maintained at <0.1 ppm  $\text{H}_2\text{O}$  and  $\text{O}_2$ .

### Characterisation

Powder X-ray diffraction (PXRD) patterns were recorded on a 9 KW Rigaku Smartlab diffractometer using  $\text{Cu K}\alpha_1$  radiation ( $\lambda = 1.54051 \text{ \AA}$ ). A customized air-tight sample holder covered with Kapton film was used to avoid severe air/moisture contact during measurement.



Chemical analyses were performed by Inductively Coupled Plasma (ICP) using a Perkin Elmer Elan 6100 DRC ICP-MS.

Time-of-flight powder neutron diffraction data were collected on the GEM high-intensity, medium-resolution instrument at ISIS, Rutherford Appleton Laboratories. Neutron scattering lengths of 0.363, 1.03, 0.566,  $-0.373$  and  $0.5803$  ( $\text{all} \times 10^{-12}$  cm) were assigned to Na, Ni, Mg, Mn, and O, respectively.<sup>32</sup>

Mn and Ni K-edge X-ray absorption near edge structure (XANES) measurements of the pristine materials were performed at the B18 beamline at the Diamond Light Source, UK. The XANES spectra were collected in transmission mode and the intensities of both the incident and transmitted X-ray beams were measured using gas-filled ionisation chambers. Mn and Ni foil were placed in front of a third ionisation chamber and were used to correct any drift in the monochromator. Three scans were performed for each sample. Athena software was used to sum the scans, calibrate and normalise the data and extract the background.  $\text{Mn}_2\text{O}_3$ ,  $\text{MnO}_2$ ,  $\text{NiO}$  and  $\text{K}_2\text{NiF}_6$  were used as references for  $\text{Mn}^{3+}$ ,  $\text{Mn}^{4+}$ ,  $\text{Ni}^{2+}$  and  $\text{Ni}^{4+}$ , respectively.

Electrodes were prepared by mixing the active material with Super S carbon and a solution of 5 wt% PVDF (polyvinylidene fluoride) in NMP (*N*-methyl-2-pyrrolidone) in a 75:15:10 weight ratio. Slurries of the mixtures were prepared by adding *ca.* 1 ml of NMP to the mixture under constant stirring for 3–4 h. The slurry was cast onto Al foil that acts as current collector in an argon-filled glovebox. Loading of active material for the galvanostatic cycling is  $2\text{--}3 \text{ mg cm}^{-2}$ . The coated foil was dried under vacuum at  $80^\circ\text{C}$  for 2 h and electrodes of 20 mm were punched out and pressed under a load of  $4 \text{ tons cm}^{-2}$ .

Galvanostatic charging/discharging tests were performed in CR2325 coin cells using 1 M  $\text{NaPF}_6$  (99.99% Sigma Aldrich) in PC (propylene carbonate) as the electrolyte solution and sodium metal as the counter electrode. Coin cells were charged/discharged at  $10 \text{ mA g}^{-1}$  in the  $2\text{--}4.5 \text{ V}$  range.

### *In operando* X-ray diffraction

Customised half cells with 3 mm diameter holes in the casing and 5 mm diameter holes in the stainless spacer were used for the construction of the coin cells for the *in operando* measurements. The coin cells contained the electrodes described above, Na metal ( $\sim 1$  mm thickness), a glass fibre separator and 1 M  $\text{NaPF}_6$  in PC (propylene carbonate) electrolyte solution. *In operando* synchrotron XRD experiments were performed within 1–2 days after cell construction. Data were collected on the Powder Diffraction beamline<sup>33</sup> at the Australian Synchrotron with a wavelength ( $\lambda$ ) of  $0.70772(2) \text{ \AA}$  for  $x = 0$  and  $x = 0.1$  and  $0.70793(2) \text{ \AA}$  for  $x = 0.2$ , where the wavelength is determined by refining a structural model with data collected on a NIST 660b  $\text{LaB}_6$  standard reference material. XRD data were collected continuously in transmission geometry every 4.4(1) minutes for the  $x = 0.1$  and  $x = 0.2$  samples and 6.4 minutes for the  $x = 0$  sample. In conjunction, the *in operando* cells were first charged to 4.5 V at relatively fast rates between  $30\text{--}100 \text{ mA g}^{-1}$  and then subsequently discharged to 2 V and charged to 4.5 V at lower rates between  $10\text{--}30 \text{ mA g}^{-1}$ . The electrode loading varied from  $1\text{--}4 \text{ mg cm}^{-2}$  and the current rates were adjusted to

accommodate this variation. PXRD and ND data were refined by the Rietveld method using the GSAS software suite with the EXPGUI software interface.<sup>34</sup>

### *Ab initio* simulations

Density functional theory (DFT) calculations were performed using the Vienna *ab initio* simulation package (VASP).<sup>35</sup> Valence electrons were described by a plane-wave basis set with a cut-off energy of 450 eV. The interactions between valence and core electrons were treated using the projector augmented-wave (PAW) method.<sup>36</sup> The *k*-space was sampled with *k*-point mesh spacing smaller than  $0.05 \text{ \AA}^{-1}$ . Spin-polarization was enabled and ferromagnetic coupling between magnetic manganese cations was assumed. Structural optimization was performed until the residue force on each atom is smaller than  $0.03 \text{ eV \AA}^{-1}$ . Similar DFT methods have been applied successfully to a range of battery materials.<sup>37–40</sup> *Ab initio* molecular dynamics (AIMD) simulations were carried out to study  $\text{Na}^+$  ion diffusion in  $\text{Na}_{0.56}\text{Ni}_{0.33}\text{Mn}_{0.67}\text{O}_2$  and  $\text{Na}_{0.56}\text{Mg}_{0.11}\text{Ni}_{0.22}\text{Mn}_{0.67}\text{O}_2$  with supercells containing 192 atoms. Each composition was first equilibrated for 10 picoseconds. Statistical properties were then obtained by the subsequent 50 ps simulations using the NVT ensemble with a Nosé–Hoover thermostat.<sup>41,42</sup> All molecular dynamics simulations were performed at 500 K with a time step of 2 femtoseconds. Gamma-point only was used in the *k*-space sampling in order to keep the computational cost affordable.

### Conflicts of interest

There are no conflicts to declare.

### Acknowledgements

P. G. B. and M. S. I. are grateful to the Engineering and Physical Sciences Research Council (EPSRC) including the SUPERGEN Energy Storage Hub for financial support (EP/L019469/1). We additionally thank the Australian Research Council, (grants DE160100237 and DP170100269) for financial support and the HPC Materials Chemistry Consortium (EP/L000202/1) for Archer supercomputer facilities. Neutron diffraction experiments were performed on the GEM beamline at the ISIS spallation source at the Rutherford Appleton Laboratory, UK. We would like to thank Dr Robert Armstrong for helpful discussions on neutron diffraction data refinements. XANES measurements were performed on the B18 beamline of Diamond Light Source, UK. The authors are grateful to A. V. Chadwick, G. Cibin and S. Ramos for contributing to XAS data collection. A component of this research was undertaken on the Powder Diffraction beamline at the Australian Synchrotron, part of the Australian Nuclear Science and Technology Organisation (ANSTO). We would like to thank James C. Pramudita for assistance with cell preparation for the synchrotron studies. Research data can be accessed on DOI: 10.5287/bodleian:wxQPqzDdd.

## References

- M. H. Han, E. Gonzalo, G. Singh and T. Rojo, A comprehensive review of sodium layered oxides: powerful cathodes for Na-ion batteries, *Energy Environ. Sci.*, 2015, **8**, 81–102.
- N. Ortiz-Vitoriano, N. E. Drewett, E. Gonzalo and T. Rojo, High performance manganese-based layered oxide cathodes: overcoming the challenges of sodium ion batteries, *Energy Environ. Sci.*, 2017, **10**, 1051–1074.
- C. Delmas, C. Fouassier and P. Hagenmuller, Structural classification and properties of the layered oxides, *Phys. B+C*, 1980, **99**, 81–85.
- Z. Lu and J. R. Dahn, Can all the lithium be removed from  $T2\text{-Li}_{2/3}[\text{Ni}_{1/3}\text{Mn}_{2/3}]\text{O}_2$ ?, *J. Electrochem. Soc.*, 2001, **148**, A710–A715.
- Z. Lu and J. R. Dahn, *In situ* X-ray diffraction study of  $P2\text{-Na}_{2/3}\text{-}[\text{Ni}_{1/3}\text{Mn}_{2/3}]\text{O}_2$ , *J. Electrochem. Soc.*, 2001, **148**, A1225–A1229.
- D. H. Lee, J. Xu and Y. S. Meng, An advanced cathode for Na-ion batteries with high rate and excellent structural stability, *Phys. Chem. Chem. Phys.*, 2013, **15**, 3304–3312.
- Y. Wang, R. Xiao, Y.-S. Hu, M. Avdeev and L. Chen,  $P2\text{-Na}_{0.6}[\text{Cr}_{0.6}\text{Ti}_{0.4}]\text{O}_2$  cation-disordered electrode for high-rate symmetric rechargeable sodium-ion batteries, *Nat. Commun.*, 2015, **6**, 1–9.
- X. Wu, G.-L. Xu, G. Zhong, Z. Gong, J. McDonald, S. Zheng, R. Fu, Z. Chen, K. Amine and Y. Yang, Insights into the effects of zinc doping on structural phase transition of P2-type sodium nickel manganese oxide cathodes for high-energy sodium ion batteries, *ACS Appl. Mater. Interfaces*, 2016, **8**, 22227–22237.
- H. Yoshida, N. Yabuuchi, K. Kubota, I. Ikeuchi, A. Garsuch, M. Schulz-Dobrickb and S. Komaba, P2-type  $\text{Na}_{2/3}\text{Ni}_{1/3}\text{-Mn}_{2/3}\text{-}x\text{Ti}_x\text{O}_2$  as a new positive electrode for higher energy Na-ion batteries, *Chem. Commun.*, 2014, **50**, 3677–3680.
- X. Wu, J. Guo, D. Wang, G. Zhong, M. J. McDonald and Y. Yang, P2-type  $\text{Na}_{0.66}\text{Ni}_{0.33}\text{-}x\text{Zn}_x\text{Mn}_{0.67}\text{O}_2$  as new high-voltage cathode materials for sodium-ion batteries, *J. Power Sources*, 2015, **281**, 18–26.
- L. Wang, Y.-G. Sun, L.-L. Hu, J.-Y. Piao, J. Guo, A. Manthiram, J. Ma and A.-M. Cao, Copper-substituted  $\text{Na}_{0.67}\text{Ni}_{0.3-x}\text{Cu}_x\text{Mn}_{0.7}\text{O}_2$  cathode materials for sodium-ion batteries with suppressed P2–O2 phase transition, *J. Mater. Chem. A*, 2017, **5**, 8752–8761.
- W. Zhao, H. Kirie, A. Tanaka, M. Unno, S. Yamamoto and H. Noguchi, Synthesis of metal ion substituted P2- $\text{Na}_{2/3}\text{-Ni}_{1/3}\text{Mn}_{2/3}\text{O}_2$  cathode material with enhanced performance for Na ion batteries, *Mater. Lett.*, 2014, **135**, 131–134.
- G. Singh, N. Tapia-Ruiz, J. M. Lopez del Amo, U. Maitra, J. W. Somerville, A. R. Armstrong, J. Martinez de Ilarduya, T. Rojo and P. G. Bruce, High Voltage Mg-Doped  $\text{Na}_{0.67}\text{Ni}_{0.3-x}\text{Mg}_x\text{Mn}_{0.7}\text{O}_2$  ( $x = 0.05, 0.1$ ) Na-Ion Cathodes with Enhanced Stability and Rate Capability, *Chem. Mater.*, 2016, **28**, 5087–5094.
- N. Yabuuchi, R. Hara, K. Kubota, J. Paulsen, S. Kumakura and S. Komaba, New electrode material for rechargeable sodium batteries: P2-type  $\text{Na}_{2/3}[\text{Mg}_{0.28}\text{Mn}_{0.72}]\text{O}_2$  with anomalously high reversible capacity, *J. Mater. Chem. A*, 2014, **2**, 16851–16855.
- N. Yabuuchi, R. Hara, M. Kajiyama, K. Kubota, T. Ishigaki, A. Hoshikawa and S. Komaba, New O2/P2-type Li-excess layered manganese oxides as promising multi-functional electrode materials for rechargeable Li/Na batteries, *Adv. Energy Mater.*, 2014, 1301453.
- J. M. Paulsen, R. A. Donabarger and J. Dahn, Layered T2-, O6-, O2-, and P2-type  $\text{A}_{2/3}[\text{M}'^{2+}_{1/3}\text{M}^{4+}_{2/3}]\text{O}_2$  bronzes, A = Li, Na; M' = Ni, Mg; M = Mn, Ti, *Chem. Mater.*, 2000, **12**, 2257–2267.
- M. Freire, N. V. Kosova, C. Jordy, D. Chateigner, O. I. Lebedev, A. Maignan and V. Pralong, A new active Li–Mn–O compound for high energy density Li-ion batteries, *Nat. Mater.*, 2016, **15**, 173.
- D. Igarashi, Y. Miyazaki and T. Kajitani, Disorder-order transitions in  $\text{Na}_x\text{CoO}_2$  ( $x \sim 0.58$ ), *Phys. Rev. B: Condens. Matter Mater. Phys.*, 2008, **78**, 184112.
- P.-F. Wang, Y. You, Y.-X. Yin, Y.-S. Wang, L.-J. Wan, L. Gu and Y.-G. Guo, Suppressing the P2–O2 phase transition of  $\text{Na}_{0.67}\text{Mn}_{0.67}\text{Ni}_{0.33}\text{O}_2$  by magnesium substitution for improved sodium-ion batteries, *Angew. Chem., Int. Ed.*, 2016, **55**, 7445–7449.
- N. Yabuuchi, M. Kajiyama, J. Iwatate, H. Nishikawa, S. Hitomi, R. Okuyama, R. Usui, Y. Yamada and S. Komaba, P2-type  $\text{Na}(x)[\text{Fe}_{(1/2)}\text{Mn}_{(1/2)}]\text{O}_2$  made from earth abundant elements for rechargeable Na batteries, *Nat. Mater.*, 2012, **11**, 512–517.
- J. Xu, D. H. Lee, R. J. Clément, X. Yu, M. Leskes, A. J. Pell, G. Pintacuda, X.-Q. Yang, C. P. Grey and Y. S. Meng, Identifying the Critical Role of Li Substitution in P2- $\text{Na}_x[\text{Li}_y\text{Ni}_z\text{Mn}_{1-y-z}]\text{O}_2$  ( $0 < x, y, z < 1$ ) Intercalation Cathode Materials for High-Energy Na-Ion Batteries, *Chem. Mater.*, 2014, **26**, 1260–1269.
- R. J. Clément, J. Billaud, A. R. Armstrong, G. Singh, T. Rojo, P. G. Bruce and C. P. Grey, Structurally stable Mg-doped P2- $\text{Na}_{2/3}\text{Mn}_{1-y}\text{MgO}_2$  sodium-ion battery cathodes with high rate performance: insights from electrochemical, NMR and diffraction studies, *Energy Environ. Sci.*, 2016, **9**, 3240–3251.
- Y. Mo, S. P. Ong and G. Ceder, Insights into Diffusion Mechanisms in P2 Layered Oxide Materials by First-Principles Calculations, *Chem. Mater.*, 2014, **26**, 5208–5214.
- N. A. Katcho, J. Carrasco, D. Saurel, E. Gonzalo, M. Han, F. Aguesse and T. Rojo, Origins of Bistability and Na Ion Mobility Difference in P2- and O3- $\text{Na}_{2/3}\text{Fe}_{2/3}\text{Mn}_{1/3}\text{O}_2$  Cathode Polymorphs, *Adv. Energy Mater.*, 2016, **7**, 1601477.
- Z.-Y. Li, R. Gao, J. Zhang, X. Zhang, Z. Hu and X. Liu, New insights into designing high-rate performance cathode materials for sodium ion batteries by enlarging the slab-spacing of the Na-ion diffusion layer, *J. Mater. Chem. A*, 2016, **4**, 3453–3461.
- M. Roger, D. J. P. Morris, D. A. Tennant, M. J. Gutmann, J. P. Goff, J.-U. Hoffman, R. Feyerherm, E. Dudzik, D. Prabhakaran, A. T. Boothroyd, N. Shannon, B. Lake and P. P. Deen, Patterning of sodium ions and the control of electrons in sodium cobaltate, *Nature*, 2006, **445**, 631–634.
- M.-H. Julien, C. de Vaulx, H. Mayaffre, C. Berthier, M. Horvatić, V. Simonet, J. Wooldridge, G. Balakrishnan,

- M. R. Lees, D. P. Chen, C. T. Lin and P. Lejay, Electronic Texture of the Thermoelectric Oxide  $\text{Na}_{0.75}\text{CoO}_2$ , *Phys. Rev. Lett.*, 2008, **100**, 096405.
- 28 G. Lang, J. Bobroff, H. Alloul, G. Collin and N. Blanchard, Spin correlations and cobalt charge states: Phase diagram of sodium cobaltates, *Phys. Rev. B: Condens. Matter Mater. Phys.*, 2008, **78**, 155116.
- 29 F. L. Ning, S. M. Golin, K. Ahilan, T. Imai, G. T. Shu and F. C. Chou,  $^{59}\text{Co}$  NMR Evidence for Charge Ordering below TCO  $\sim 51$  K in  $\text{Na}_{0.5}\text{CoO}_2$ , *Phys. Rev. Lett.*, 2008, **100**, 086405.
- 30 F. M. F. de Groot, M. Grioni, J. C. Fuggle, J. Ghijsen, G. A. Sawatzky and P. Petersen, Oxygen 1s X-ray-absorption edges of transition-metal oxides, *Phys. Rev. B: Condens. Matter Mater. Phys.*, 1989, **40**, 5715.
- 31 P. A. Cox, *Transition Metal Oxides: An Introduction to Their Electronic and Properties*, Oxford University Press, 1992.
- 32 V. F. Sears, Neutron scattering lengths and cross sections, *Neutron News*, 1992, **3**, 26.
- 33 K. S. Wallwork, B. J. Kennedy and D. Wang, The high resolution powder diffraction beamline for the Australian Synchrotron, *AIP Conf. Proc.*, 2006, 879.
- 34 A. C. Larson and R. B. Von Dreele in *Los Alamos National Laboratory Report LAUR 86-748*, 1994; B. H. J. Toby, *Appl. Crystallogr.*, 2001, **34**, 210–213.
- 35 G. Kresse and J. Furthmüller, Efficient iterative schemes for *ab initio* total-energy calculations using a plane-wave basis set, *Phys. Rev. B: Condens. Matter Mater. Phys.*, 1996, **54**, 11169–11186.
- 36 P. E. Blöchl, Projector augmented-wave method, *Phys. Rev. B: Condens. Matter Mater. Phys.*, 1994, **50**, 17953–17979.
- 37 M. S. Islam and C. A. J. Fisher, Lithium and sodium battery cathode materials: computational insights into voltage, diffusion and nanostructural properties, *Chem. Soc. Rev.*, 2014, **43**, 185–204.
- 38 A. R. Armstrong, C. Lyness, P. Panchmatia, M. S. Islam and P. G. Bruce, The lithium intercalation process in the low voltage lithium battery anode  $\text{Li}_{1+x}\text{V}_{1-x}\text{O}_2$ , *Nat. Mater.*, 2011, **10**, 223.
- 39 H. Chen and M. S. Islam, Lithium Extraction Mechanism in Li-Rich  $\text{Li}_2\text{MnO}_3$  Involving Oxygen Hole Formation and Dimerization, *Chem. Mater.*, 2016, **28**, 6656.
- 40 S. P. Ong, V. L. Chevrier, G. Hautier, A. Jain, C. Moore, S. Kim, X. Ma and G. Ceder, *Energy Environ. Sci.*, 2011, **4**, 3680.
- 41 S. Nosé, A unified formulation of the constant temperature molecular dynamics methods, *J. Chem. Phys.*, 1984, **81**, 511–519.
- 42 W. G. Hoover, Canonical dynamics: equilibrium phase-space distribution, *Phys. Rev. A*, 1985, **31**, 1695–1697.